Accepted for publication in Journal of Fluids Engineering

VORTEX DYNAMICS AND LOW-PRESSURE FLUCTUATIONS IN THE TIP-CLEARANCE FLOW

Donghyun You[†,*], Meng Wang[‡], Parviz Moin[†], and Rajat Mittal[§]

[†]Center for Turbulence Research, Stanford University, Stanford, CA 94305

[‡]Department of Aerospace and Mechanical Engineering, University of Notre Dame, Notre Dame, IN 46556

[§]Department of Mechanical and Aerospace Engineering, George Washington University, Washington, DC 20052

ABSTRACT

The tip-clearance flow in axial turbomachines is studied using large-eddy simulation with particular emphasis on understanding the unsteady characteristics of the tip-leakage vortical structures and the underlying mechanisms for cavitation-inducing low-pressure fluctuations. Systematic and detailed analysis of the velocity and pressure fields has been made in a linear cascade with a moving end-wall. The generation and evolution of the tip-leakage vortical structures have been investigated throughout the cascade using mean streamlines and λ_2 contours. An analysis of the energy spectra and space-time correlations of the velocity fluctuations suggests that the tip-leakage vortex is subject to a pitchwise low frequency wandering motion. Detailed statistics of the pressure fields has been analyzed to draw inferences on cavitation. The regions of low pressure relative to the mean values coincide with regions of strong pressure fluctuations, and the regions are found to be highly correlated with the vortical structures in the tip-leakage flow, particularly in the tip-leakage and tip-separation vortices.

Keywords: tip-clearance flow, tip-leakage vortex, cavitation, turbomachinery, large-eddy simulation, vortex dynamics

[*]Corresponding author. Tel: +1-650-725-1821; fax: +1-650-725-3525; email: dyou@stanford.edu.

NOMENCLATURE

C	Chord length
C_a	Axial chord length
f	Frequency
p	Pressure
Re	Reynolds number
t	Time
U	Time-averaged streamwise velocity
U_∞	Inflow freestream velocity
u_i	x_i component of velocity
u_τ	Wall-shear velocity
u	Streamwise velocity
v	Pitchwise velocity
w	Spanwise velocity
x_i	Cartesian coordinates
x	Streamwise coordinate
y	Pitchwise coordinate
z	Spanwise coordinate
ν	Kinematic viscosity
Δ	Grid spacing
ω	Angular frequency
$()^+$	Quantity in wall-unit
$()'$	Fluctuation component

1 INTRODUCTION

The radial clearance between a rotor-blade tip and casing wall in a turbomachine is indispensable for its operation. However, its existence has been a major source of unfavorable flow phenomena. Complicated vortical structures are generated by the tip-clearance flow and its interactions with the end-wall boundary layer, the blade wake, and the neighboring blade. The tip-clearance vortical structures often induce rotating instabilities and blockage in the flow passage which result in severe performance loss and subsequent stall of axial compressors [1, 2]. Also, in a transonic compressor, the interaction between passage shock and tip-clearance flow is implicated in the degradation of efficiency as well as vibrations and noise generation [3]. These issues have motivated a number of experimental and computational investigations of the compressor tip-clearance flow, and some basic understanding has been achieved (e.g. [4–11]).

On the other hand, in hydraulic turbomachines such as submarine propulsors and liquid pumps, the existence of tip clearance is considered to be a cause for cavitation, which can result in loud acoustic noise, performance deterioration, and the erosion of blades and casing wall (e.g. [8,9,12–14]). In order to understand the mechanisms for cavitation, it is necessary to study the detailed vortex dynamics in the rotor-blade wake and tip-clearance region and the associated low-pressure events.

In the 1950's, Rains [12] investigated cavitation phenomenon in an axial flow pump and observed that the tip-leakage vortex forms from the leading edge of the blade, and convects downstream across the passage for a range of tip gaps of $0.2\% \sim 5.2\%$ chord. Later, in an axial pump, Zierke et al. [13] showed the existence of a trailing-edge tip-separation vortex that migrates radially upward along the trailing edge. This trailing-edge tip-separation vortex then moves along the circumferential direction near the casing and in the opposite direction of blade rotation. They also established the trajectory of the tip-leakage vortex core with the observation of the unsteadiness of the vortex, subject to wandering and kinking motions in the passage and downstream. Similar unsteadiness is also discussed in the work of Goto [9]. Pressure fluctuation and turbulence measurements made adjacent to the casing wall show the track of developing tip-leakage vortex as a strip of

high turbulence levels which grows across the passage [8]. The pressure frequency spectra of Goto [9] showed a general rise in high-frequency spectral levels in the vicinity of the casing, suggesting the presence of small scale turbulence in the region containing the tip-leakage vortex. Although these and other earlier investigations have revealed gross features of the tip-leakage vortical structures and related flow phenomena, the detailed dynamics of the vortical structures such as the tip-leakage vortex and tip-separation and induced vortices, and influence of the end-wall vortical structures on the low pressure, pressure fluctuations, and cavitation are poorly understood.

In recent years, a series of experiments has been performed at Virginia Tech. to make detailed measurements of the flow field in a low speed linear compressor cascade with stationary and moving end-walls [15–20]. Mean velocity, vorticity, turbulent kinetic energy, and frequency energy spectra were measured downstream of the rotor blades. Wang and Devenport [16] employed a moving end-wall and found noticeable difference in the mean velocity and Reynolds stress distributions from the experiments which utilized a stationary end-wall [15]. Kuhl [18] and Ma [20] examined the effects of upstream vortex pairs on the downstream tip-leakage vortex. Employing a stationary end-wall, Wenger et al. [17] performed two-point measurements of the turbulent fluctuations in the downstream tip-leakage flow, and showed conclusively that the tip-leakage vortex is not subject to low-frequency pitchwise "wandering" motions. On the other hand, an experiment employing a moving end-wall showed a noticeable low-frequency spectral peak in the pitchwise velocity energy spectra [16]. However, no further investigation regarding the origin and mechanism of this low-frequency peak were made.

These experiments [15, 16, 18, 20] have provided useful information regarding the flow as well as valuable data for validating computational techniques. However, since the measurements were limited to the flow field at least one and a half chord lengths downstream from the trailing edge, they could not shed light on the upstream flow features which are critically important. In addition, these experiments could not provide information regarding the mean pressure and pressure fluctuations in the cascade passage region. Ma [20] performed pressure measurements in the far downstream planes using microphones but indicated that the measured mean pressure and pressure fluctuations could be affected by the noise in the cascade tunnel, probe interference, and wind induced noise inside the microphone.

Experimental measurements of the tip-leakage flow in the vicinity of the tip gap very close to the end-wall are generally difficult due to technical and safety issues. In addition, the strong unsteadiness of the tip-leakage flow limits the applicability of conventional Reynolds-averaged Navier-Stokes (RANS) approaches in a computational study. These difficulties have been major obstacles to a detailed understanding of the tip-leakage flow physics leading to cavitation. Although, the gross feature of the tip-leakage vortex has been known for some time, a deeper quantitative understanding of the dynamics of the tip-leakage vortical structures and their interaction with the end-wall boundary layer is needed to elucidate the tip-leakage cavitation mechanisms.

In this study, the tip-leakage flow, particularly in regions not studied experimentally, is investigated using data generated by large-eddy simulation (LES). The objective is to gain an improved understanding of the unsteady characteristics of the vortical structures present in the typical tip-clearance configuration, and the cavitation-inducing low-pressure fluctuations associated with the tip-leakage vortical structures. In order to gain such an understanding, it is necessary to study the detailed turbulence dynamics in the rotor-blade wake and the tip-clearance region and to examine the space-time correlations of the coherent turbulence structures present in the end-wall tip-leakage flow. A detailed investigation regarding mean pressure and pressure fluctuations is also carried out to understand tip-leakage cavitation in hydraulic turbomachines.

The computational methodology is described in section 2. Details of the vortex dynamics, velocity and pressure fluctuations, and cavitation inception are discussed in section 3, followed by conclusions in section 4.

2 COMPUTATIONAL METHODOLOGY

2.1 Numerical Method

The numerical algorithm and solution method are described in detail in Ref. [21]. Here, we summarize the main features of the methodology. The three-dimensional, unsteady, incompressible Navier-Stokes equations are solved in a generalized coordinate system on a structured grid in conjunction with a Smagorinsky type dynamic subgrid-scale (SGS) model. Given the fully inhomogeneous nature of the flow, a Lagrangian dynamic SGS model, which averages the model coefficient along

the flow pathlines [22], is employed.

The integration method used to solve the governing equations is based on a fully-implicit fractional-step method which avoids the severe time-step restriction in the tip-clearance region. All terms including cross-derivative diffusion terms are advanced in time using the Crank-Nicolson method and are discretized in space by energy-conserving second-order central-differencing. A Newton iterative method is used to solve the discretized nonlinear equations. For the pressure Poisson equation, an efficient multigrid procedure, which is a combination of the line and red-black Gauss-Seidel multigrid method is used. This method is particularly appropriate for parallelization. The simulation code is parallelized using OpenMP.

2.2 Computational Setup

The flow configuration, coordinate definition, and measurement planes for investigating the flow field are schematically shown in Fig. 1. The present study is focused on a linear cascade with a moving end-wall at the bottom of the tip gap that matches the experimental setup of Wang and Devenport [16]. A single blade passage is considered, with periodic boundary conditions in the y-direction to mimic the flow in the interior of a cascade. The computational domain is of size $L_x \times L_y \times L_z = 1.8C \times 0.929C \times 0.5C$, where C is the blade chord. The mesh size used for the final simulation is $449 \times 351 \times 129$.

The important parameters for the base simulation are as follows: The size of the tip clearance is $0.0165C$, the blade pitch is $0.9C$, and the blade span is $0.5C$. The blade has a relatively high stagger-angle of about 57 degrees. The Reynolds number of this flow is $400,000$ based on the chord and inflow free-stream velocity, and the inflow turbulent boundary layer has a Reynolds number of 780 based on the momentum thickness. The momentum thickness of the inflow is 11.8% of the tip-gap size. The speed of moving end-wall is 90.8% of the inflow free-stream velocity. The coordinate variables are normalized using the blade axial chord C_a $(= 0.546C)$.

The inflow turbulent boundary-layer data is provided using the method of Lund et al. [23], modified to account for the fact that the mean flow direction is not perpendicular to the inflow/outflow plane. No-slip boundary conditions are applied

along the rotor blade and moving end-wall, and the convective boundary condition is applied at the exit boundary.

The difficulty with grid topology in the tip-clearance region is overcome by an approach which combines an immersed boundary technique [24] with a structured grid in a generalized coordinate system. The advantage of using a curvilinear mesh with an immersed-boundary method is that we can generate grid lines almost parallel to the blade surface. This ensures an adequate resolution on the boundary layers, and allows periodic boundary conditions to be applied on the curved upper and lower boundaries. The immersed boundary method when used with the curvilinear mesh, obviates a complex mesh topology and allows us to use a simple single-block mesh [21]. In addition to this, the high stagger angle in the experimental setup necessitates the use of very skewed mesh, which requires fine control of mesh parameters such as the stretching ratio and the aspect ratio, and an adequate formulation of nonlinear convection terms to avoid numerical instability (see Refs. [25, 26] for more details).

3 RESULTS AND DISCUSSION

3.1 Effects of Resolution and SGS model

In general, the grid resolution on the blade surface is reasonable compared to previous LES studies of wall bounded turbulent flows using similar numerical methods [27]. The grid spacings based on the chord in the streamwise, pitchwise, and spanwise directions are $9.9\times10^{-4} \leq \Delta x/C \leq 1.4\times10^{-2}$, $9.8\times10^{-4} \leq \Delta y/C \leq 6.5\times10^{-3}$, and $4.6\times10^{-4} \leq \Delta z/C \leq 1.2\times10^{-2}$, respectively. In wall units, the blade-surface resolution in the region of primary interest is within the range $\Delta x^+ \leq 50$, $\Delta y^+ \leq 3$, and $\Delta z^+ \leq 30$ (Δz^+ increases up to 90 far from the tip-gap region.). As seen in Fig. 2, the pressure distribution over the blade surface is generally comparable with that of experiment with stationary end-wall [15] and indicates that the current mesh topology is capable of resolving the gross features of the flow. The grid resolution normal to the end-wall is in the range of $0.3 \leq \Delta z^+ \leq 2.1$. In the directions parallel to the end-wall, Δx^+ and Δy^+ are generally less than 50, except in a small end-wall region where the maximum values reach $90 \sim 100$ because of the strong effect of the tip-leakage vortex on the boundary layer. In the $y-z$ plane at $x/C_a = 0.6$, more than 50 grid points in the pitchwise and spanwise

directions are allocated across the tip-leakage vortex core. The grid spacing based on the chord and the resolution in wall units in the important regions are presented in Tables 1 and 2. The resolution in Kolmogorov units (η), which is estimated by an evaluation of the production and assuming equilibrium, is in the range of $\Delta x/\eta, \Delta y/\eta \leq 40$, and $\Delta z/\eta \leq 10$ in the end-wall region, while $\Delta z/\eta$ increases up to 110 far from the end-wall. Figure 3 shows that ratios of the grid spacing to the Kolmogorov lengthscale in the end-wall parallel directions are relatively high underneath the blade-tip and around the tip-leakage vortex core (Figs. 3(a) and (b)), while the ratio of the spanwise grid spacing to the Kolmogorov lengthscale is relatively high on the suction surface boundary layer far from the end-wall (Fig. 3(c)).

Prior to this simulation, coarser grid simulations had been carried out to determine the resolution requirements, and the final mesh was subsequently constructed using this information. To investigate the grid sensitivity, simulations of flow through the cascade without tip-gap, which are less expensive than the present simulation, were performed with refined meshes in all three directions, and it was confirmed that results are relatively insensitive to the grid resolution. Figure 4 is an example of the study which shows reasonable robustness of the mean velocity with respect to the grid resolution. Further details of the grid resolution study and comparisons with experimental data were reported in [21].

The simulation is advanced in time with the maximum Courant-Friedrichs-Lewy (CFL) number equal to 4 which corresponds to $\Delta t U_\infty/C \approx 0.73 \times 10^{-3}$ where U_∞ is the incoming freestream velocity. The effect of CFL number on the instantaneous solution has been examined in simulations performed with CFL numbers of 1.5, 2.5, 4, and 5. As seen in Figure 5, in terms of the amplitude and phase, the variation of the streamwise velocity is reasonably robust up to the CFL number of 4. The maximum CFL number occurs near the pressure side of the blade tip where the strong downward flow passes across the dense mesh region aligned parallel to the blade tip and to the blade surface as seen in Fig. 6, and except for this location, the CFL number is much less than 1. The severe time-step restriction in the dense mesh region is avoided by employing a fully-implicit integration method. In wall units, the time-step ($\Delta t^+ = \Delta t u_\tau^2/\nu$) is generally far less than 0.8. Each time-step requires a wallclock time of about 200 seconds when 128 CPUs of an SGI Origin 3800 are used. The results which will be discussed below are obtained by integrating the governing equations over a time interval of about $30C/U_\infty$.

The flow field near the suction surface necessitates enhanced eddy viscosity compared to the pressure side where the eddy-viscosity becomes negligible because of very low level of turbulence activity. Except for the relatively coarse mesh region in the blade wake far from the end-wall, the peak mean eddy viscosity is usually less than 10 times the value of the molecular viscosity, which is similar to the magnitude observed in the LES study of backward facing step flow [27]. Figure 7 shows the resolved and total Reynolds shear stress profiles along the spanwise direction at $x/C_a = 0.6$ and $y/C_a = 1.51$, and apparently indicates that the contribution of the subgrid-scale shear stress to the total Reynolds shear stress is reasonably small.

3.2 Development of End-Wall Vortical Structures

The pressure difference between the pressure and suction sides of the blade tip generates a strong jet flow through the blade tip gap. The tip-leakage jet produces the tip-leakage vortex, tip-separation vortices, and several other secondary vortices such as induced vortices. Although many aspects of the tip-leakage vortex have been reported in the literature, details regarding the evolutionary features of the tip-leakage vortex and other secondary vortices have not been well understood. This understanding is crucial in predicting and eventually controlling the cavitation phenomena in hydraulic tip-clearance configurations since the behavior and pattern of tip-leakage cavitation are closely related to those of the end-wall vortical structures.

In this section, streamlines are utilized to visualize the end-wall vortical structures and investigate their behaviors along their evolutionary paths as shown in Fig. 8. Figure 9 shows mean streamlines in the end-wall normal cross-sectional planes shown in Fig. 8 as viewed by an observer looking upstream. In this plot, a pitchwise velocity which corresponds to the moving end-wall velocity is subtracted from the mean flow field to elucidate the end-wall vortices. Among the distinct vortical structures, the tip-leakage vortex which is found near the suction side of the blade dominates the field. To the right of the tip-leakage vortex, induced vortices are noticed. A pitchwise stretched recirculating region is also observed underneath the blade tip. This circulation is closely related to the tip-separation vortices near the trailing edge.

The generation and evolution of the end-wall vortical structures observed in Fig. 9 are more extensively discussed along with Fig. 10, which shows λ_2 contours representing vortices in a series of $y-z$ planes along the streamwise direction as viewed by an observer looking upstream. It is generally difficult to identify various vortical structures with different convection speeds embedded in the tip-leakage flow using streamlines. The λ_2 vortex identification method makes it easier to clearly identify the vortical structures in the end-wall normal planes at various streamwise locations. Since the λ_2 contours cannot provide the rotational direction of a vortex, the rotational direction for each end-wall vortex is determined using streamlines as shown in Fig. 9. At about 7% axial chord, a secondary vortex is induced by the tip separation and by the moving end-wall. This secondary vortex rotates in a counter-clock wise direction and corresponds to the induced vortex 2 in Fig. 9. The tip-leakage vortex begins to be identified at around $x/C_a = 11\% \sim 20\%$ axial chord. In this range of axial chord, a small secondary vortex is also observed slightly above the tip-leakage vortex near the blade suction surface. However, the strength of the secondary vortex is weak and is not observed in further downstream locations. At 26% axial chord, the strong tip-leakage vortex and the induced vortex 2 which is generated in the upstream induce another secondary vortex (induced vortex 1 in Fig. 9(b) and (c)) between them. The induced vortex 1 is found to rotate in the opposite direction of the other vortices and its rotational strength increases with the strength of the tip-leakage vortex. During the course of its evolution, the strength of the first induced vortex decreases rapidly after 30% axial chord. The mechanism for generation of the third secondary vortex (induced vortex 3 in Fig. 9) is unclear. It is observable from the plane at 11% axial chord location, but its rotational strength is much weaker than those of the other vortices. It may be induced by the end-wall motion which drags the inflow turbulent boundary layer in the positive pitchwise direction.

The strength of the induced vortices is significantly reduced at about 37% axial chord, where the rotational strength of the tip-leakage vortex reaches its maximum. Then, the strength of the tip-leakage vortex decreases with axial chord and pitchwise stretching of the vortex becomes significant ($x/C_a = 0.40$ and 0.44). As seen at 51% and 59% axial chords, the induced vortices are still identifiable near the pressure side of the neighboring blade, but their strengths are much reduced and they eventually dissipate. Muthanna and Devenport [15] and Wang and Devenport [16] also observed the induced vortices,

but they could not clarify the mechanisms for their generation, propagation, and decay. In their experiments, it was assumed that the induced vortices disappear from the end-wall by being engulfed by the tip-leakage vortex, not by dissipation.

From 51% axial chord location, another noticeable vortical structure is found on the blade suction surface which corresponds to the blade boundary layer separation. The tip-separation vortices become significant near the suction side of the blade tip after the mid-chord. Unlike the tip-leakage vortex which is formed by the roll-up of the tip-leakage jet, the tip-separation vortices are generated by the circulating region which is dragged by the tip-leakage jet (Fig. 9).

An interesting development of the tip-leakage vortex is found at about 73% axial chord. At this location, the pitchwise stretched tip-leakage vortex breaks up near the end-wall and its shape becomes more complicated. However, even at further downstream locations ($x/C_a \geq 0.81$), the core of the main part of the tip-leakage vortex is still well defined. Near the trailing edge ($x/C_a = 0.95$), the end-wall vortical field becomes highly complicated due to the tip-leakage vortex separation, the tip-separation vortices, and the blade wake near the blade tip. The end-wall region further downstream is characterized by the interaction of these vortical structures.

3.3 Two-Point Correlations of Velocity Fluctuations

In this section, the spatial and temporal behaviors of the coherent structures present in the tip-leakage flow are examined more quantitatively. Two-point correlations of velocity fluctuations are computed to elucidate the coherent structures embedded in the end-wall tip-leakage flow. Figure 11 shows the mean streamwise velocity contour in a $y-z$ plane at $x/C_a = 1.51$ as seen by an observer looking upstream and the location (**A**) where the two-point correlations of velocity fluctuations are computed. Vertical bundles of the mean streamwise velocity contour are present in the wakes of rotor blades, and the tip-leakage vortices are found as velocity deficits near the end-wall. In this plane, the mean streamwise velocity and turbulence intensity profiles are compared with the experimental data along the spanwise direction at $y/C_a = 1.35$, and are shown in Fig. 12. Considering the experimental difficulty in measuring near wall flow quantities on a moving end-wall and the mass leakage in the experiment (see Refs. [21, 28] for more detailed discussion on this issue.), the agreement is favorable.

In order to obtain energy spectra of velocity fluctuations and space-time correlations which will be discussed later in this section, about 15,000 samples of the streamwise, pitchwise, and spanwise velocity components were collected over a time interval $TU_\infty/C \sim 20$. The Lomb periodogram technique [29] with an oversampling factor of four was used to perform the spectral analysis of unevenly sampled data. Note that the time step is not constant because the filtered Navier-Stokes equations are integrated in time using a fully-implicit method with a fixed CFL number.

Figure 13 shows normalized energy spectra of velocity fluctuations computed in the core of the tip-leakage vortex (see Fig. 11 for the location). The spectral density and frequency are normalized using the inflow free-stream velocity (U_∞) and blade chord (C). Energy spectra for the three velocity components show broadband characteristics of the turbulent fluctuations present in the end-wall tip-leakage flow. Energy spectra in all three velocity components predict an inertial subrange which is typically described with the slope of $-5/3$. In addition, the present results at $x/C_a = 1.51$ show favorable agreement with the experimental data provided by Wang and Devenport [16].

In the core of the tip-leakage vortex inside the cascade passage ($x/C_a = 1.51$), noticeable spectral peaks are observed in the energy spectra of the pitchwise velocity component, while no indications of significant low-frequency coherent structures are found in the energy spectra of other velocity components. The spectral peaks are observed to be concentrated in the non-dimensional frequency of 1.5. The existence of the spectral peak in the pitchwise velocity fluctuations has also been reported by Wang and Devenport [16]. However, it was unclear in this experiment as to what caused the low-frequency spectral peak. This finding was not in accordance with the observations in the experiments employing a stationary end-wall [15] where low-frequency spectral peaks were not observed except for the peak found in the blade wake. By analyzing two-point correlations of the velocity fluctuations in the end-wall tip-leakage flow, Wenger et al. [17] concluded that the low-frequency coherent (or wandering) motion of the tip-leakage vortex is not present in the experiments employing a stationary end-wall.

In order to investigate the possibility that the blade wake causes the observed low-frequency coherent motion, the energy spectra of velocity fluctuations in the blade wake at a location of $x/C_a = 1.51, y/C_a = 2.2$, and $z/C_a = 0.9$, which is far from the end-wall, are computed. In Fig. 14, the present LES results are also compared with the experimental data [15]. The LES

results show earlier drops of energy in the high frequency region, especially of the spanwise velocity component. This is related to the relatively coarse resolution along the span far away from the end-wall (see Fig. 3(c)). Energy spectra for the pitchwise velocity fluctuations shows a prominent spectral peak which indicates existence of periodic shedding of the blade wake. However, in both the present LES and experiment [16], the measured frequency for the wake shedding is found to be around $fC/U_\infty = 5 \sim 6$ which is quite different from the peak frequency ($fC/U_\infty = 1.5$) measured in the end-wall tip-leakage vortex. Therefore, the shedding of the blade wake does not directly influence the pitchwise coherent motion in the end-wall tip-leakage flow.

Energy spectra of velocity fluctuations are processed by an inverse Fourier transform to obtain the normalized space-time correlation coefficients,

$$R_{u_iu_i}(y,\Delta y,z,\Delta z,\Delta\tau) = \frac{\sum_\omega E_{u_iu_i}(y,\Delta y,z,\Delta z,\omega)e^{-i\omega t}}{\overline{u_i^2(y,z)}}, \tag{1}$$

where Δy, Δz, and $\Delta\tau$ represent spatial separations in the pitchwise and spanwise directions, and the temporal separation, respectively. $i = 1, 2$, and 3 correspond to the streamwise, pitchwise, and spanwise directions, respectively.

Considering that the spectral peak appears only in the pitchwise velocity fluctuations, the space-time correlation coefficients for velocity fluctuations are computed as a function of pitchwise and temporal separations. Figure 15 shows the space-time correlations of the pitchwise velocity fluctuations at the same location as for Fig. 13. The space-time correlations show sign changes along the pitchwise separation axis indicating the existence of a large-scale coherent structure. The pitchwise extent of the correlation is roughly equal to the pitchwise extent of the tip-leakage vortex. In the present study, for small values of pitchwise separation, the major axis of the correlation contours is found to be nearly parallel to the time separation axis. This reflects the existence of a coherent motion of the large-scale structure corresponding to the long time delay.

The present correlations are different from those found by Wenger *et al.* [17] in the stationary end-wall case. They found

that the correlations are concentrated in an elliptical region whose major axis extends diagonally in the pitchwise-temporal separation plane. The major axis of the ellipse extends five to six times farther than its minor axis, and no noticeable correlations along the time separation axis are observed for zero pitchwise separation. They concluded that the coherent motions responsible for these correlations are not wandering.

Figure 16 shows the oscillatory feature of the tip-leakage vortex in terms of the instantaneous low pressure iso-surfaces at two different times separated by the half period of the pitchwise oscillation. It is found that the frequency of the oscillatory motion of the tip-leakage vortex corresponds to the frequency observed in the energy spectra. The exact source of the low-frequency spectral peak is not clearly identified. Considering that the frequency is much lower than the typical wake shedding frequencies observed in the blade trailing-edge and the blade tip, the shear layer instability in the tip-leakage jet flow is considered as the most probable cause for the low-frequency spectral peak.

3.4 Mean Pressure and Pressure Fluctuations

The dynamic behaviors of the end-wall vortical structures are also reflected in the distributions of mean pressure and pressure fluctuations. As already discussed in section 3.1, an insight regarding the end-wall vortical structures will be useful in predicting the pattern of tip-leakage cavitation. In the single phase flow approach employed here, the resulting pressure field is most relevant to the cavitation inception. The mean pressure fields obtained from the present LES are shown in Fig. 17 in the $x-y$ planes along the span. In the plane very close to the end-wall ($z/C_a = 0.01$), low pressure is observed in the upstream portion of the tip-leakage vortex and underneath the blade tip. The existence of the tip-leakage vortex is reflected in the pressure iso-contour lines in further downstream locations as well. Comparisons of the contour lines of mean pressure distribution in planes $z/C_a = 0.01$ and 0.025 suggest that the mean pressure distributions across the blade tip are qualitatively and quantitatively similar. It is also noted that the mean pressure on the pressure side of the blade tip near the end-wall is significantly higher while that on the suction side of the blade tip is relatively low. The pressure difference is the driving force for the tip-leakage jet across the tip gap.

At $z/C_a = 0.1$, negative mean pressure (or of which levels are smaller than the mean pressure) is found on the blade suction surface as well as along the tip-leakage vortex. Further away from the end-wall ($z/C_a = 0.5$), only the blade suction surface and its vicinity attain negative pressure. The magnitude of the negative pressure is significantly smaller than that of the end-wall tip-leakage vortex. From this perspective, it is most likely that cavitation occurs in the upstream portion of the tip-leakage vortex and underneath the tip gap.

The intensity of the pressure fluctuations is also an important factor in triggering cavitation, especially in the region where the mean pressure is close to the vapor pressure. Due to the pressure fluctuations, the instantaneously observed extent of the cavitation is usually more significant. The intensity of pressure fluctuations is shown in Fig. 18 at four $x-y$ planes along the span. High levels of pressure fluctuations are found in the tip-leakage vortex and underneath the blade tip. Also, a small region near the leading edge on the pressure side of the blade shows fluctuations due to the separation near the leading edge ($z/C_a = 0.01$ and 0.025). The intensity of pressure fluctuations on the pressure surface near the leading edge and on the suction surface near the trailing edge become significant in planes further away from the end-wall ($z/C_a \geq 0.1$). Compared to the pressure fluctuations in those regions, the pressure fluctuations along the blade wake appear to be small.

The mean pressure and pressure fluctuations are also examined in a number of $y-z$ planes along the streamwise direction as shown in Figs. 19 and 20. At about the 10% axial chord location (Fig. 19(a)), no significant low pressure region is found near the end-wall since no significant vortical structures are generated. Although a small scale weak induced vortex is observed at this location, its strength is insufficient to produce a noticeable pressure drop in the vortex core (see Fig. 10). A significant pressure drop due to the formation of the tip-leakage vortex is observed at about $30 \sim 40\%$ axial chord (Fig. 19(b)) where the minimum pressure is located exactly in the core of the tip-leakage vortex (also see Fig. 10).

At 50% axial chord (Fig. 19(c)), the tip-leakage vortex core corresponds to the low pressure region as well defined by the pressure iso-contours. At a downstream plane ($x/C_a = 1.51$, Fig. 19(d)), the core of the tip-leakage vortex is not a region of negative pressure, while the region underneath the blade tip still attains negative pressure but with significantly reduced magnitude. At a $y-z$ plane near the trailing edge ($x/C_a = 0.9$, Fig. 19(e)), the pressure contours still reflect the existence of

the tip-leakage vortex. However the pressure in this location has already increased above the free-stream value.

Figure 20 shows the intensity of the pressure fluctuations in $y-z$ planes along the streamwise direction. The intensity of pressure fluctuations appears to be the maximum at about 30% axial chord (Fig. 20(b)). In the upstream location at 10% axial chord (Fig. 20(a)), significant levels of pressure fluctuations due to boundary layer separation on the blade pressure surface are observed. At 50% axial chord (Fig. 20(c)), the tip-leakage vortex is still well defined as a region of high levels of pressure fluctuations, but the region between the tip-leakage vortex and the suction side of the blade tip generates enhanced pressure fluctuations. This may be caused by the strong turbulence and vorticity productions in the tip-leakage jet as discussed in detail in Ref. [25]. The high level of pressure fluctuations in these regions may cause vibration of the blade and casing, as well as significant noise. In Figs. 17-20, it is obvious that the region of upstream tip-leakage vortex, especially at around $30 \sim 40\%$ axial chord, is most susceptible to cavitation and generates the most significant pressure fluctuations. Therefore, in the present configuration, cavitation can be best mitigated by diminishing the strength and coherency of the tip-leakage vortex at around $30 \sim 40\%$ axial chord.

3.5 Cavitation Inception

The low pressure regions are known to be susceptible to cavitation. Figure 21 shows an example of cavitation inception analysis in a plane parallel to the end-wall inside the tip gap using the minimum tension criterion proposed by Joseph [30].

This criterion is based on the normal stress of the fluid and the critical vapor pressure:

$$B_{ii} = \tau_{ii} - p + p_c > 0, \tag{2}$$

where τ_{ii} is the normal stress, p is local pressure and p_c is the pressure in the cavity. Only the resolved normal-stress components defined as $\tau_{ii} = 2\mu\partial\bar{u}_i/\partial x_i$, where $\bar{u}_i$ is the filtered velocity, are considered while the filtered pressure is corrected to account for the trace of the subgrid stress. For this example, p_c of 0.01 is used, assuming the cavitation number of 0.02

based on the cascade inlet pressure. If all three components of the stress B_{11}, B_{22} and B_{33} are positive, a cavity will open.

Instantaneous and time-averaged contours of $B = 1/3(B_{11} + B_{22} + B_{33})$ are plotted in Figs. 21(a) and (b), respectively, in regions where all three components are positive. High levels of B in both the instantaneous and time-averaged contours are concentrated in the tip-leakage region. In particular, the tip-leakage vortex appears as the dominant source of cavitation. The tip-separation vortex is less important even though it involves comparable low pressure (see Figs. 17(a) and (b)). This is due to the high positive values of the normal stress τ_{ii} in addition to the strong low pressure found in the tip-leakage vortex.

4 CONCLUSIONS

The tip-clearance flow in axial turbomachines has been studied using large-eddy simulation with an emphasis on understanding the unsteady characteristics of the tip-leakage vortical structures and the underlying mechanisms for cavitation-inducing low-pressure fluctuations in the vicinity of the tip-gap. The generation and evolution of the tip-leakage vortical structures have been investigated throughout the cascade using mean streamlines and λ_2 contours. Among the distinct vortical structures, the tip-leakage vortex dominates the end-wall region. The induced vortices are active in the upstream end-wall region while the tip-separation vortices become significant near the suction side of the blade tip after the mid-chord. In the present configuration, the tip-leakage vortex is initiated at around $15\% \sim 20\%$ axial chord, and the evolution of the tip-leakage vortex is found to be closely related to the generation and decay of the induced vortices. Interestingly, the tip-leakage vortex is observed to spin off a part of it at about 73% axial chord due to the pitchwise end-wall motion. Although this feature of the tip-leakage vortex was not seriously considered in the literature, the tip-leakage vortex separation and its interaction with other end-wall vortices makes the downstream end-wall vortical region extremely active and complex.

To examine the spatial and temporal characteristics of the coherent structures present in the tip-leakage flow, two-point correlations of the velocity fluctuations were computed. In general, the energy spectra of the three velocity components show broadband characteristics, while a noticeable spectral peak is particularly observed in the energy spectra of the pitchwise velocity fluctuations. Analysis of the vortex shedding frequency in the blade wake and space-time correlations of the velocity

fluctuations in the end-wall tip-leakage flow suggest that a pitchwise wandering motion of the tip-leakage vortex is the cause for the low-frequency spectral peak.

The dynamic behaviors of the end-wall vortical structures are also reflected in the distributions of mean pressure and pressure fluctuations. Detailed examination of the mean pressure field revealed that cavitation is most likely in the upstream portion of the tip-leakage vortex and underneath the tip gap. A significant pressure drop due to the formation of the tip-leakage vortex is observed at about $30 \sim 40\%$ axial chord where the minimum pressure coincides with the core of the tip-leakage vortex, and the intensity of pressure fluctuations appears to be at the maximum. The $30 \sim 40\%$ axial chord is also found to be the location of the strongest portion of the tip-leakage vortex in terms of the λ_2 contours.

Based on the characteristics of the mean and fluctuating pressure, it is obvious that the region of the upstream tip-leakage vortex, especially at around $30 \sim 40\%$ axial chord, is most susceptible to cavitation. The high activity of the pressure fluctuations in these regions may also appear as a source of strong vibration of the blade and casing as well as significant levels of noise. Therefore, it is expected that a control device which can effectively diminish the strength and coherence of the tip-leakage vortex at around 30% axial chord location may also lead to reduced the cavitation, noise, and vibration.

ACKNOWLEDGMENT

The authors acknowledge the support of the Office of Naval Research under Grant No. N00014-99-1-0389, with Dr. Ki-Han Kim as program manager. Computer time was provided by a Challenge Project Grant (C82) from the U.S. Department of Defense (DoD) High Performance Computing Modernization Program (HPCMP) through Army Research Laboratory (ARL) and Aeronautical Systems Center (ASC) Major Shared Resource Centers (MSRC). The authors would also like to thank Professor William Devenport of VPI for providing experimental data and helpful discussions.

REFERENCES

[1] Furukawa, M., Saiki, K., Nagayoshi, K., Kuroumaru, M., and Inoue, M., 1998. "Effects of stream surface inclination on tip leakage flow fields in compressor rotors". *Journal of Turbomachinery,* **120** , pp. 683–694.

[2] Mailach, R., Lehmann, I., and Vogeler, K., 2001. "Rotating instabilities in an axial compressor originating from the fluctuating blade tip vortex". *Journal of Turbomachinery,* **123** , pp. 453–463.

[3] Suder, K. L., 1998. "Blockage development in a transonic, axial compressor rotor". *Journal of Turbomachinery,* **120** , pp. 465–476.

[4] Lakshminarayana, B., and Ravindranath, A., 1982. "Interaction of compressor-rotor blade wake with wall boundary layer/vortex in the end-wall boundary layer". Journal of Engineering for Power, **104** (2) April , pp. 467–478.

[5] Lakshminarayana, B., Pouagare, M., and Davino, R., 1982. "Three-dimensional flow-field in the tip region of a compressor rotor passage, part 1: mean velocity profiles and annulus wall boundary layer". *Journal of Engineering for Power,* **104** October , pp. 760–771.

[6] Pandya, A., and Lakshminarayana, B., 1983. "Investigation of the tip-clearance flow inside and at the exit of a compressor rotor passage. Part 1: mean velocity field". Journal of Engineering for Power, **105** (1) , pp. 1–12.

[7] Lakshminarayana, B., Sitaram, N., and Zhang, J., 1986. "End-wall and profile losses in a low-speed axial flow compressor rotor". *Journal of Engineering for Gas Turbines and Power,* **108** , pp. 22–31.

[8] Inoue, M., Kuroumaru, M., and Fukuhara, M., 1986. "Behavior of tip-leakage flow behind an axial compressor rotor". *Journal of Engineering for Gas Turbines and Power,* **108** , pp. 7–14.

[9] Goto, A., 1992. "Three-dimensional flow and mixing in an axial flow compressor with different rotor tip clearance". *Journal of Turbomachinery,* **114** , pp. 675–685.

[10] Stauter, R. C., 1993. "Measurements of the three-dimensional tip region flow field in an axial compressor". *Journal of Turbomachinery,* **115** , pp. 468–475.

[11] Lakshminarayana, B., Zaccaria, M., and Marathe, B., 1995. "The structure of tip clearance flow in axial flow compres-

sors". *Journal of Turbomachinery,* **117** , pp. 336–347.

[12] Rains, D. A., 1954. *Tip clearance flows in axial compressors and pumps*. PhD thesis, Division of Engineering and Applied Science, California Institute of Technology, Pasadena, California.

[13] Zierke, W. C., Farrell, K. J., and Straka, W. A., 1995. "Measurement of the tip clearance flow for a high-Reynolds-number axial-flow rotor". *Journal of Turbomachinery,* **117** , pp. 522–532.

[14] Laborde, R., Chantrel, P., and Mory, M., 1997. "Tip clearance and tip vortex cavitation in an axial flow pump". *Journal of Fluids Engineering,* **119** , pp. 680–685.

[15] Muthanna, C., and Devenport, W. J., 2004. "Wake of a compressor cascade with tip gap. Part 1. Mean flow and turbulence structure". AIAA Journal, **42** (11) , pp. 2320–2331.

[16] Wang, Y., and Devenport, W. J., 2004. "Wake of a compressor cascade with tip gap. Part 2. Effects of endwall motion". AIAA Journal, **42** (11) , pp. 2332–2340.

[17] Wenger, C. W., Devenport, W. J., Wittmer, K. S., and Muthanna, C., 2004. "Wake of a compressor cascade with tip gap. Part 3. Two-point statistics". AIAA Journal, **42** (11) , pp. 2341–2346.

[18] Kuhl, D. D., 2001. Near wall investigation of three dimensional turbulent boundary layers. Master's thesis, Department of Aerospace and Ocean Engineering, Virginia Polytechnic Institute and State University, Blacksburg, Virginia, August.

[19] de la Riva, D. H., 2001. Turbulence interaction in a highly staggered cascade-propulsor configuration. Master's thesis, Department of Aerospace and Ocean Engineering, Virginia Polytechnic Institute and State University, Blacksburg, Virginia, April.

[20] Ma, R., 2003. *Unsteady turbulence interaction in a tip leakage flow downstream of a simulated axial compressor rotor*. PhD thesis, Department of Aerospace and Ocean Engineering, Virginia Polytechnic Institute and State University, Blacksburg, Virginia, June.

[21] You, D., Mittal, R., Wang, M., and Moin, P., 2004. "Computational methodology for large-eddy simulation of tip-clearance flows". AIAA Journal, **42** (2) February , pp. 271–279.

[22] Meneveau, C., Lund, T. S., and Cabot, W. H., 1996. "A Lagrangian dynamic subgrid-scale model of turbulence". *Journal of Fluid Mechanics,* **319** , pp. 233–242.

[23] Lund, T. S., Wu, X., and Squires, K. D., 1998. "Generation of turbulent inflow data for spatially-developing boundary layer simulations". *Journal of Computational Physics,* **140** , pp. 233–258.

[24] Fadlun, E. A., Verzicco, R., Orlandi, P., and Mohd-Yusof, J., 2000. "Combined immersed-boundary finite-difference methods for three-dimensional complex flow simulations". *Journal of Computational Physics,* **161** , pp. 35–60.

[25] You, D., Moin, P., Wang, M., and Mittal, R., 2004. Study of tip clearance flow in a turbomachinery cascade using large eddy simulation. Report TF-86, Department of Mechanical Engineering, Stanford University, Stanford, California, May.

[26] You, D., Mittal, R., Wang, M., and Moin, P., 2006. "Analysis of stability and accuracy of finite-difference schemes on a skewed mesh". *Journal of Computational Physics,* **213** , pp. 184–204.

[27] Akselvoll, K., and Moin, P., 1995. Large eddy simulation of turbulent confined coannular jets and turbulent flow over a backward facing step. Report TF-63, Department of Mechanical Engineering, Stanford University, Stanford, California, February.

[28] Khorrami, M. R., Li, F., and Choudhan, M., 2002. "Novel approach for reducing rotor tip-clearance-induced noise in turbofan engines". AIAA Journal, **40** (8) , pp. 1518–1528.

[29] Press, W. H., Teukolsky, S. A., Vetterling, W. T., and Flannery, B. P., 1992. *Numerical Recipes*. Cambridge University Press.

[30] Joseph, D. D., 1998. "Cavitation and the state of stress in a flowing liquid". *Journal of Fluid Mechanics,* **366** , pp. 367–378.

[31] Jeong, J., and Hussain, F., 1995. "On the identification of a vortex". *Journal of Fluid Mechanics,* **285** , pp. 69–94.

LIST OF TABLES

LIST OF FIGURES

Figure 1. (a) Flow configuration and coordinate system for the tip-clearance flow and (b) measurement planes for investigating the flow field and definitions of velocity coordinates.

Figure 2. Surface pressure coefficient at $z/C_a = 0.916$. —— , LES; • , experiment [15].

Figure 3. Resolution in Kolmogorov units (η) in a $y-z$ plane at $x/C_a = 0.7$. (a) $\Delta x/\eta$; (a) $\Delta y/\eta$; (a) $\Delta z/\eta$.

Figure 4. Mean velocity, U/U_∞, profiles on the suction surface. —— , $897 \times 701 \times 16$ mesh; - - - - , $449 \times 351 \times 8$ mesh. The profiles at $x/C_a = 0.50$ and 0.99 are shifted by 1 and 2, respectively.

Figure 5. Time-histories of the streamwise velocity at $x/C_a = 0.7$, $y/C_a = 1.3$, and $z/C_a = 0.1$ using different CFL numbers. —— , CFL=1.5; - - - - , CFL=4; ····· , CFL=5.

Figure 6. (a) Mean streamlines and (b) contour plot of CFL number distribution in a $y-z$ plane at $x/C_a = 0.7$. In (a), every third and second point are shown in y and z directions, respectively.

Figure 7. Profiles of Reynolds shear stresses along the spanwise direction at $(x/C_a, y/C_a) = (0.6, 1.51)$. —— , total stress; - - - - , resolved stress. The profiles of $\overline{u'w'}/U_\infty^2$ and $\overline{v'w'}/U_\infty^2$ are shifted by 0.025 and 0.05, respectively.

Figure 8. Locations of the end-wall normal planes in which the mean streamlines in Fig. 9 are visualized.

Figure 9. Mean streamlines showing vortical structures in the end-wall region in $y^* - z$ planes.

Figure 10. Generation and evolution of end-wall vortical structures along the streamwise direction visualized using the λ_2 vortex identification method [31].

Figure 11. Contour plot of mean streamwise velocity in a $y-z$ plane at $x/C_a = 1.51$ and location where the energy spectra in Fig. 13 and space-time correlations in Fig. 15 are measured. y_{wake} denotes the location of peak deficit in the blade wake.

Figure 12. Profiles of the mean streamwise velocity (U/U_∞) and Reynolds normal stresses ($(\overline{u'u'}, \overline{v'v'}, \overline{w'w'})/U_\infty^2 \times 10^2$) along the spanwise direction at $(x/C_a, y/C_a) = (1.51, 1.35)$. —— , LES; • , experiment [16]. The profiles of $\overline{u'u'}/U_\infty^2 \times 10^2$, $\overline{v'v'}/U_\infty^2 \times 10^2$, and $\overline{w'w'}/U_\infty^2 \times 10^2$ are shifted by 1, 2, and 3, respectively.

Figure 13. One-dimensional frequency spectra of velocity fluctuations at the location A in Fig. 11. (a) E_{uu}; (b) E_{vv}; (c) E_{ww}.

—— , LES; • , experiment [16].

Figure 14. One-dimensional frequency spectra of velocity fluctuations in the blade wake at $x/C_a = 1.51, y/C_a = 2.2$ and $z/C_a = 0.9$. (*a*) E_{uu}; (*b*) E_{vv}; (*c*) E_{ww}. —— , LES; • , experiment [15].

Figure 15. Contour plot of two-point correlations of the pitchwise velocity fluctuations as a function of the pitchwise spatial and temporal separations in the location A in Fig. 11. Contours are from -1 to 1 with increments of 0.1.

Figure 16. Instantaneous low pressure ($p/\rho U_\infty^2 = -0.2$) iso-surfaces showing a low-frequency wandering motion of the tip-leakage vortex. (*a*) t_0; (*b*) $t_0 + 0.33C/U_\infty$.

Figure 17. Contour plots of mean pressure in $y-z$ planes along the z-direction. (*a*) $z/C_a = 0.01$; (*b*) $z/C_a = 0.025$; (*c*) $z/C_a = 0.1$; (*d*) $z/C_a = 0.5$.

Figure 18. Contour plots of $\overline{p'p'}$ in $x-y$ planes along the z-direction. (*a*) $z/C_a = 0.01$; (*b*) $z/C_a = 0.025$; (*c*) $z/C_a = 0.1$; (*d*) $z/C_a = 0.5$.

Figure 19. Contour plots of mean pressure in $y-z$ planes along the x-direction. (*a*) $x/C_a = 0.1$; (*b*) $x/C_a = 0.3$; (*c*) $x/C_a = 0.5$; (*d*) $x/C_a = 0.7$; (*e*) $x/C_a = 0.9$.

Figure 20. Contour plots of $\overline{p'p'}$ in $y-z$ planes along the x-direction. (*a*) $x/C_a = 0.1$; (*b*) $x/C_a = 0.3$; (*c*) $x/C_a = 0.5$; (*d*) $x/C_a = 0.7$; (*e*) $x/C_a = 0.9$.

Figure 21. Contours of (*a*) instantaneous and (*b*) time-averaged cavitation criterion, $B = 1/3(B_{11} + B_{22} + B_{33})$, in a plane inside the tip gap at $z/C_a = 0.01$.

x/C_a	$\Delta x/C$	Δx^+	$\Delta y/C$	Δy^+	$\Delta z/C$	Δz^+
0.2	0.0025	8.074 (9.341)	0.0004	1.29 (1.50)	0.0045	14.53 (16.81)
0.4	0.0031	10.09 (16.02)	0.0004	1.30 (2.07)	0.0045	14.65 (23.25)
0.6	0.0032	10.73 (18.23)	0.0004	1.34 (2.28)	0.0045	15.09 (25.64)
0.8	0.0045	12.60 (28.13)	0.0004	1.12 (2.50)	0.0045	12.60 (28.13)

Table 1. Grid spacing and resolution along the blade suction (pressure) surface at $z/C_a = 0.2$.

$\Delta x/C$	Δx^+	$\Delta y/C$	Δy^+	$\Delta z/C$	Δz^+
$0.001 \sim 0.0138$	$1.82 \sim 95$	$0.0009 \sim 0.0066$	$1.2 \sim 100$	0.000046	$0.3 \sim 2.1$

Table 2. Grid spacing and resolution on the end wall.

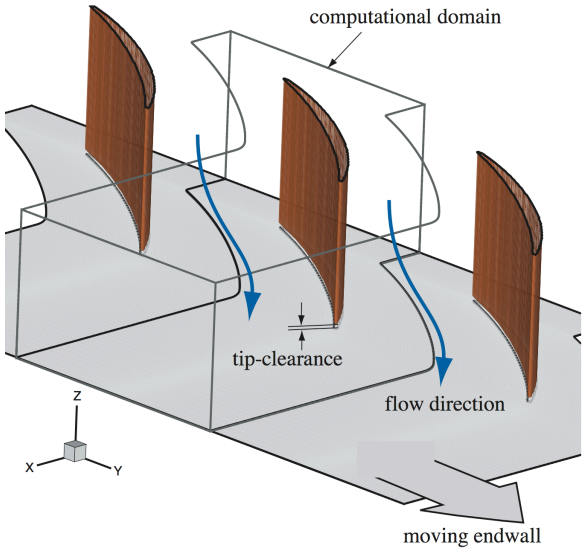

(*a*)

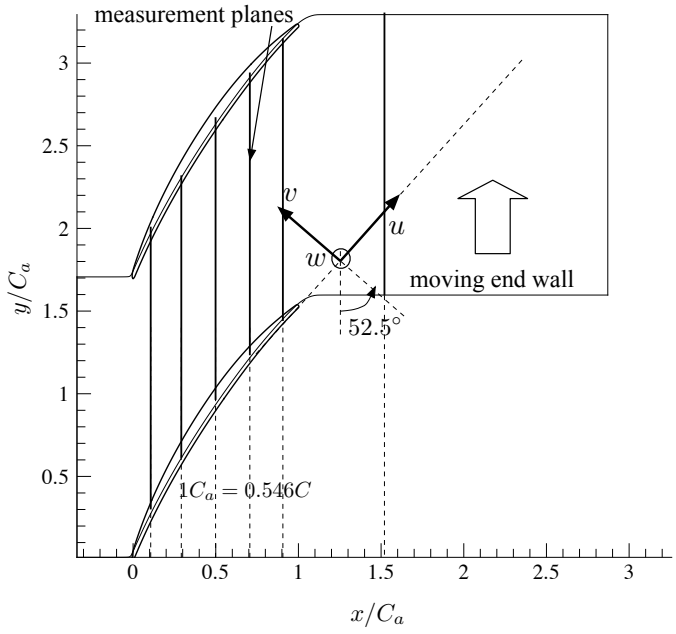

(*b*)

Figure 1. (*a*) Flow configuration and coordinate system for the tip-clearance flow and (*b*) measurement planes for investigating the flow field and definitions of velocity coordinates.

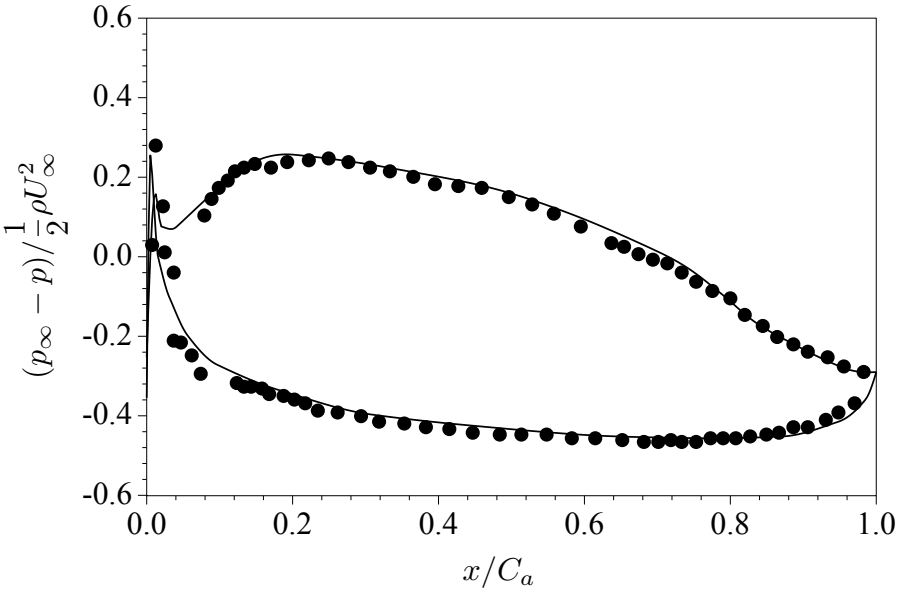

Figure 2. Surface pressure coefficient at $z/C_a = 0.916$. ——— , LES; ● , experiment [15].

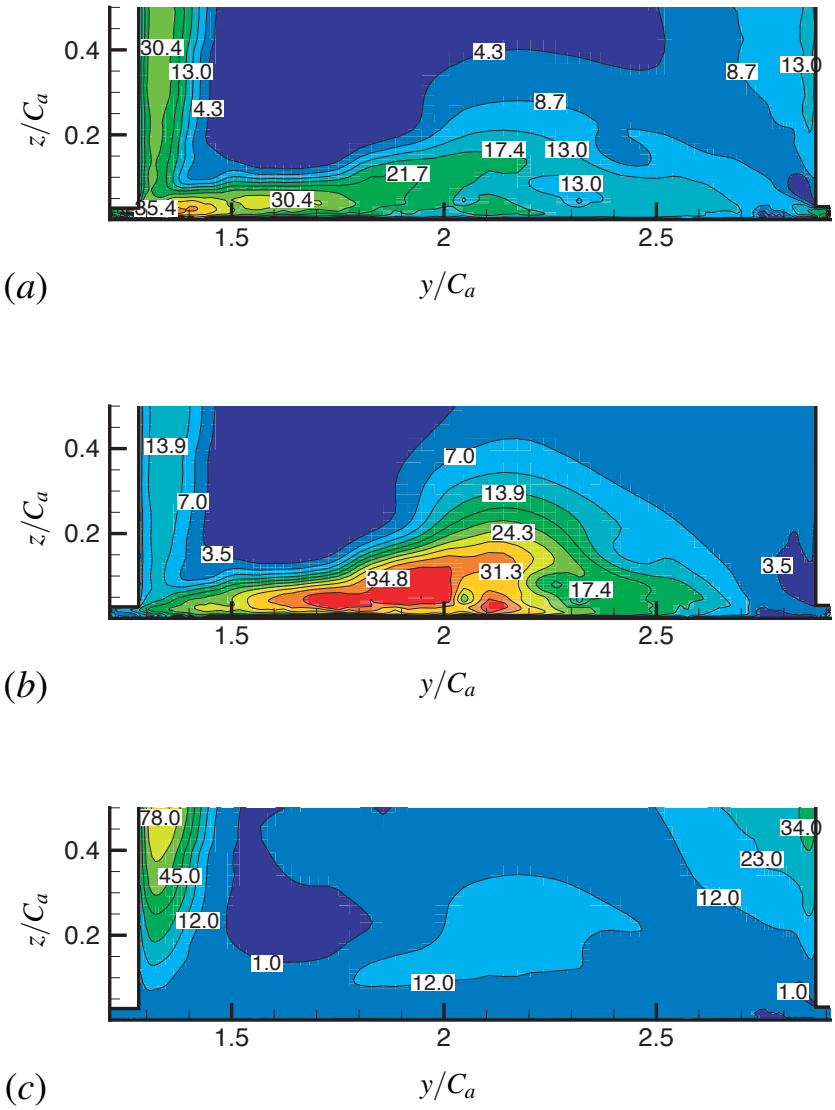

Figure 3. Resolution in Kolmogorov units (η) in a $y-z$ plane at $x/C_a = 0.7$. (*a*) $\Delta x/\eta$; (*a*) $\Delta y/\eta$; (*a*) $\Delta z/\eta$.

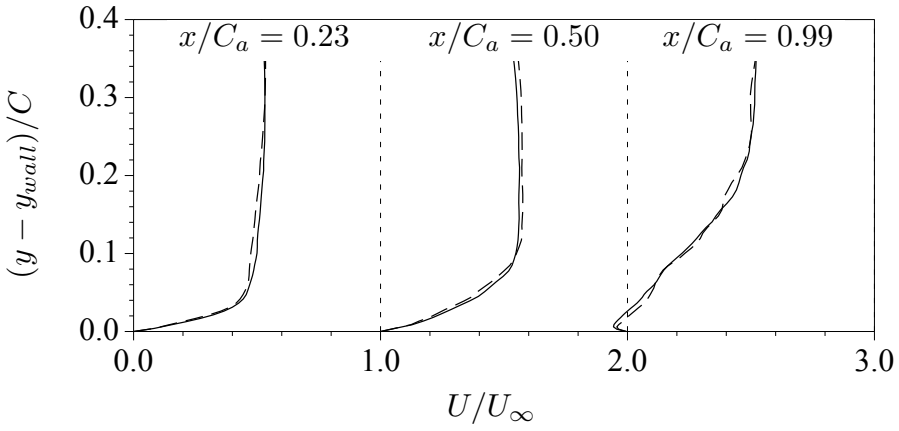

Figure 4. Mean velocity, U/U_∞, profiles on the suction surface. ——— , $897 \times 701 \times 16$ mesh; - - - - , $449 \times 351 \times 8$ mesh. The profiles at $x/C_a = 0.50$ and 0.99 are shifted by 1 and 2, respectively.

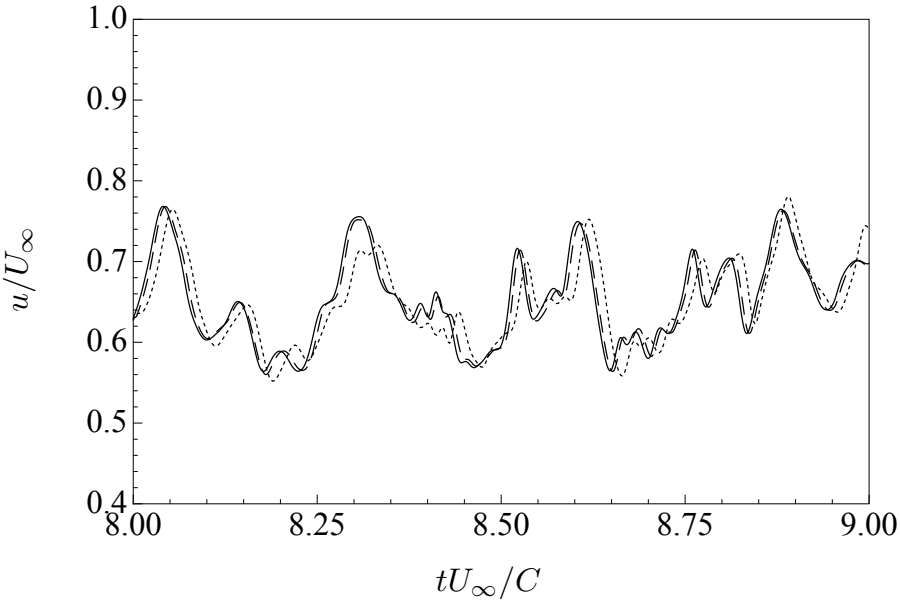

Figure 5. Time-histories of the streamwise velocity at $x/C_a = 0.7$, $y/C_a = 1.3$, and $z/C_a = 0.1$ using different CFL numbers. ——— , CFL=1.5; − − − − , CFL=4; ····· , CFL=5.

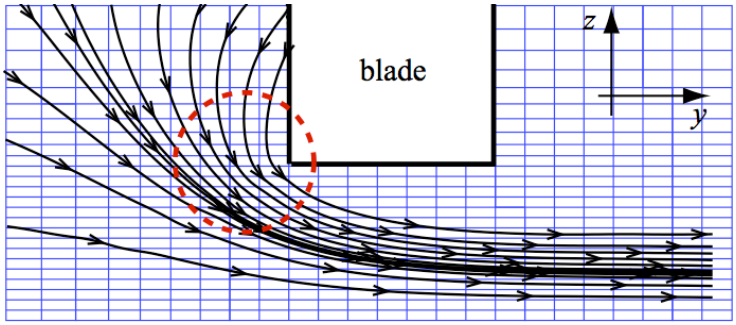

(a)

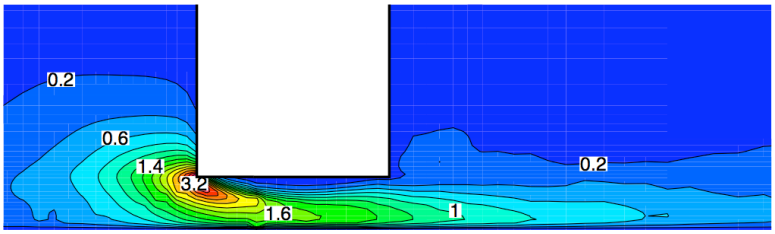

(b)

Figure 6. (a) Mean streamlines and (b) contour plot of CFL number distribution in a $y-z$ plane at $x/C_a = 0.7$. In (a), every third and second point are shown in y and z directions, respectively.

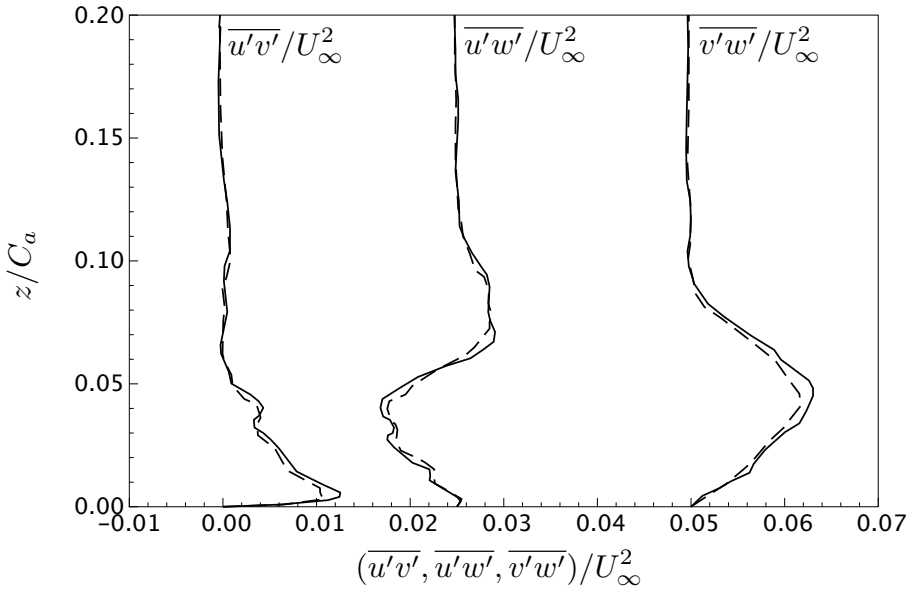

Figure 7. Profiles of Reynolds shear stresses along the spanwise direction at $(x/C_a, y/C_a) = (0.6, 1.51)$. ——— , total stress; – – – – , resolved stress. The profiles of $\overline{u'w'}/U_\infty^2$ and $\overline{v'w'}/U_\infty^2$ are shifted by 0.025 and 0.05, respectively.

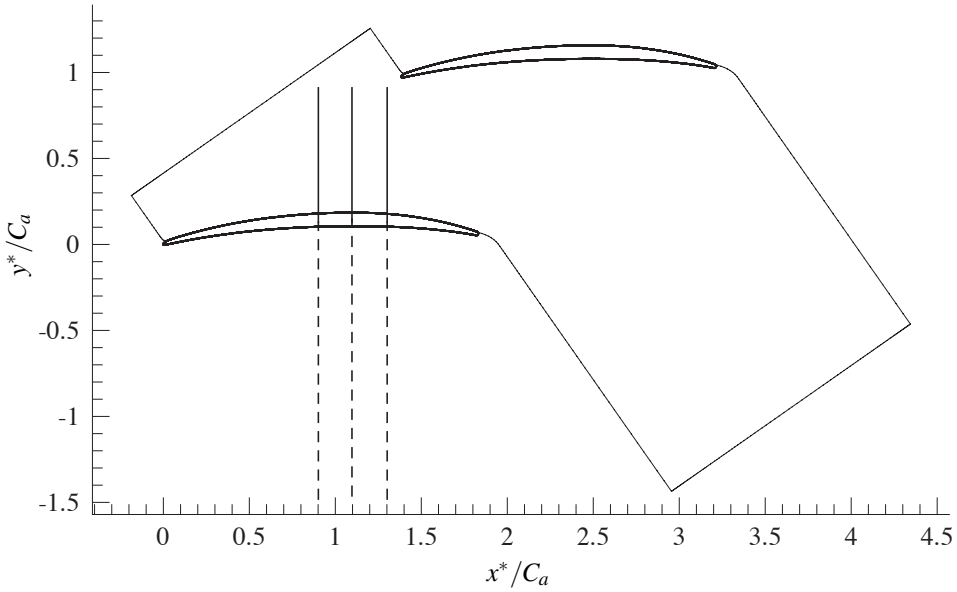

Figure 8. Locations of the end-wall normal planes in which the mean streamlines in Fig. 9 are visualized.

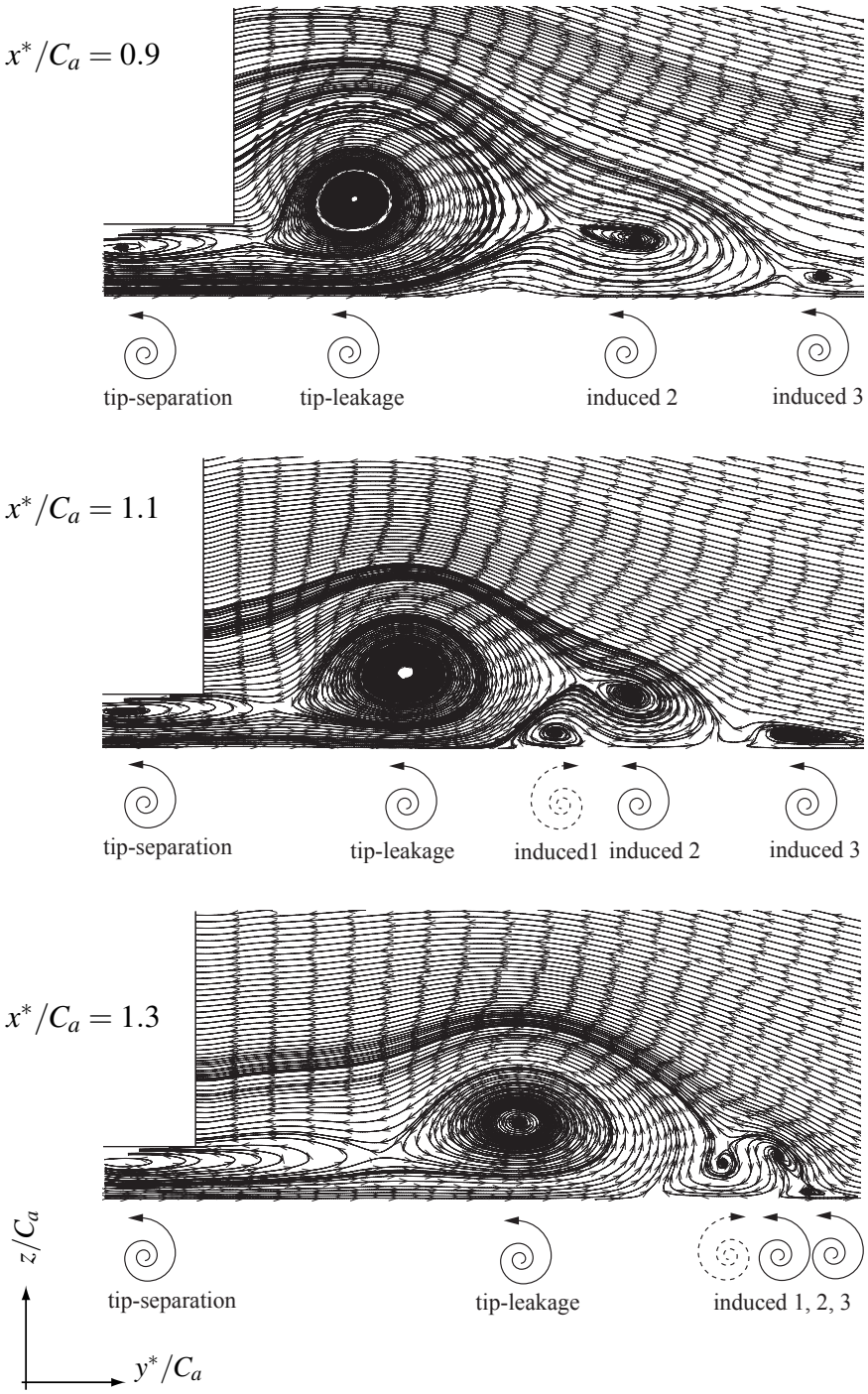

Figure 9. Mean streamlines showing vortical structures in the end-wall region in $y^* - z$ planes.

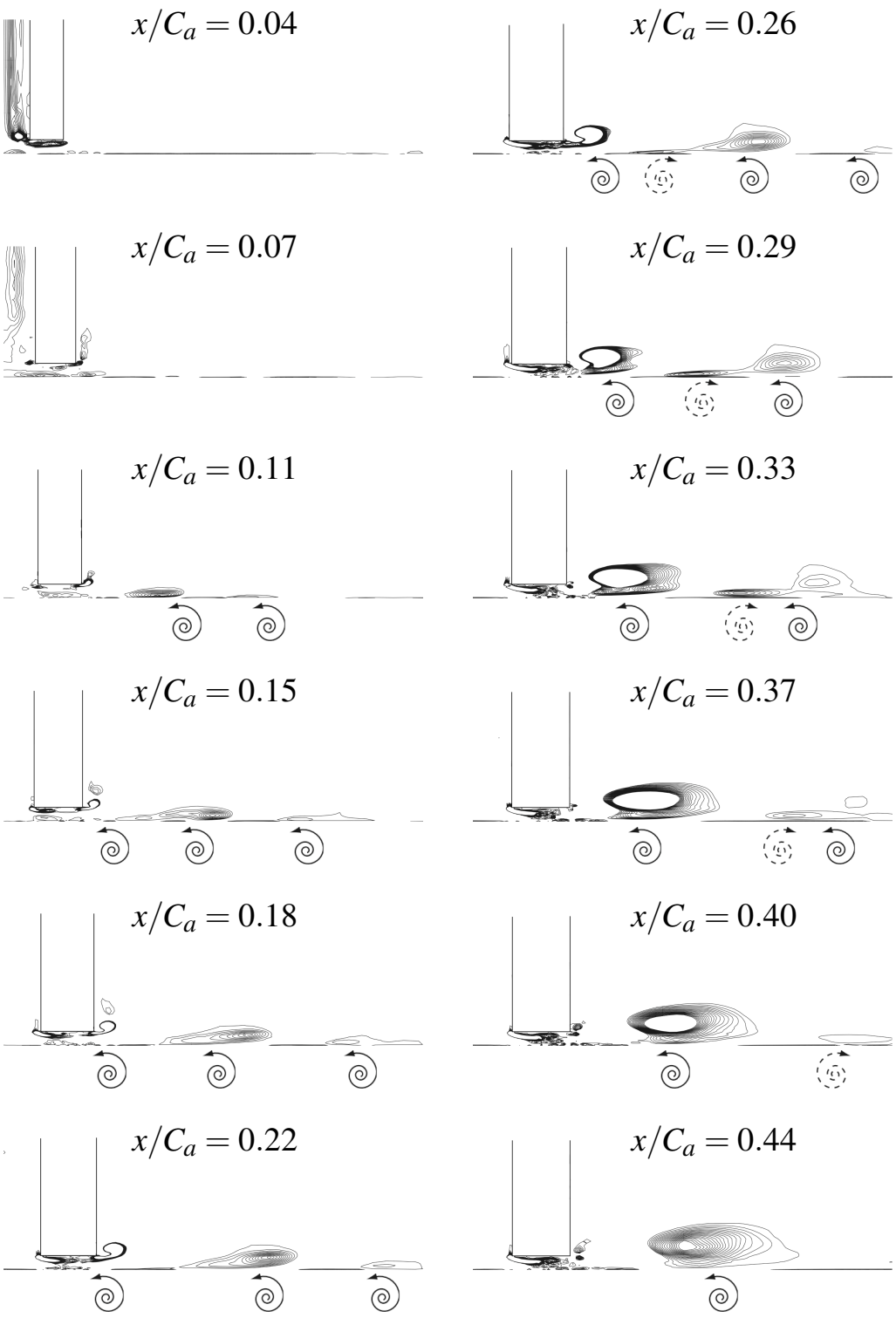

Figure 10. For caption see the following page.

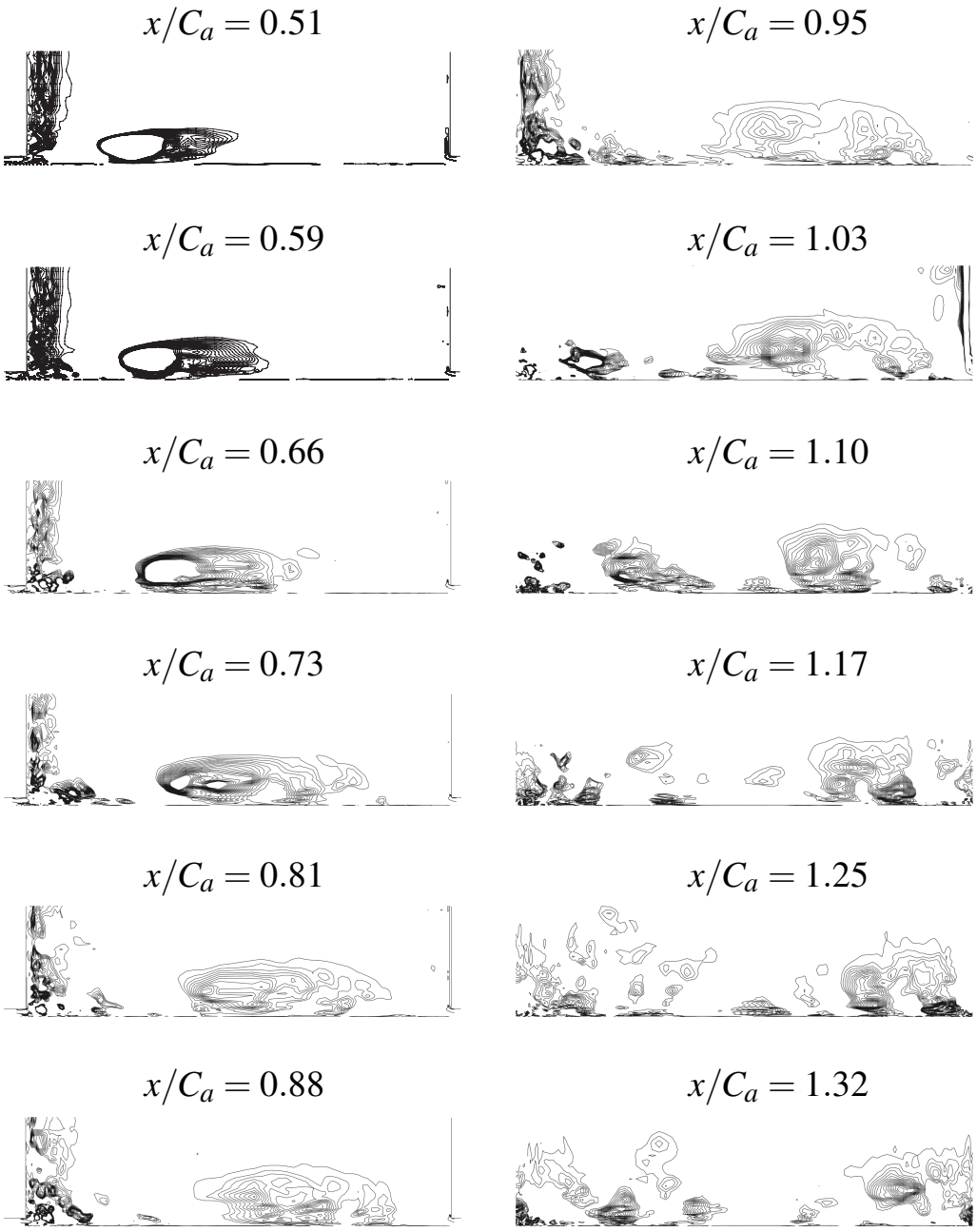

Figure 10. Generation and evolution of end-wall vortical structures along the streamwise direction visualized using the λ_2 vortex identification method [31].

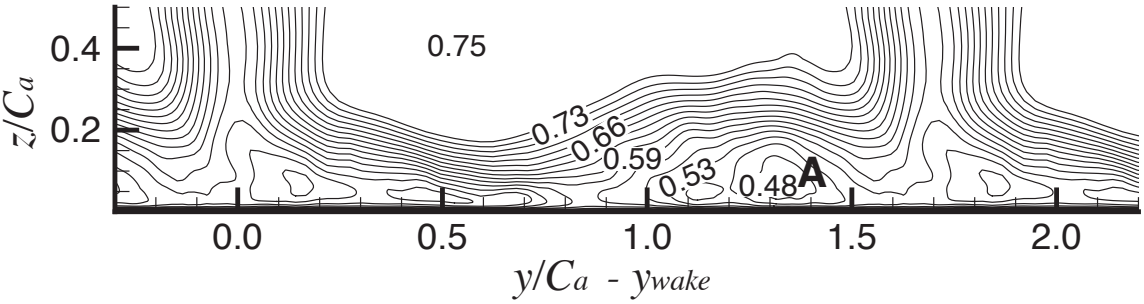

Figure 11. Contour plot of mean streamwise velocity in a $y-z$ plane at $x/C_a = 1.51$ and location where the energy spectra in Fig. 13 and space-time correlations in Fig. 15 are measured. y_{wake} denotes the location of peak deficit in the blade wake.

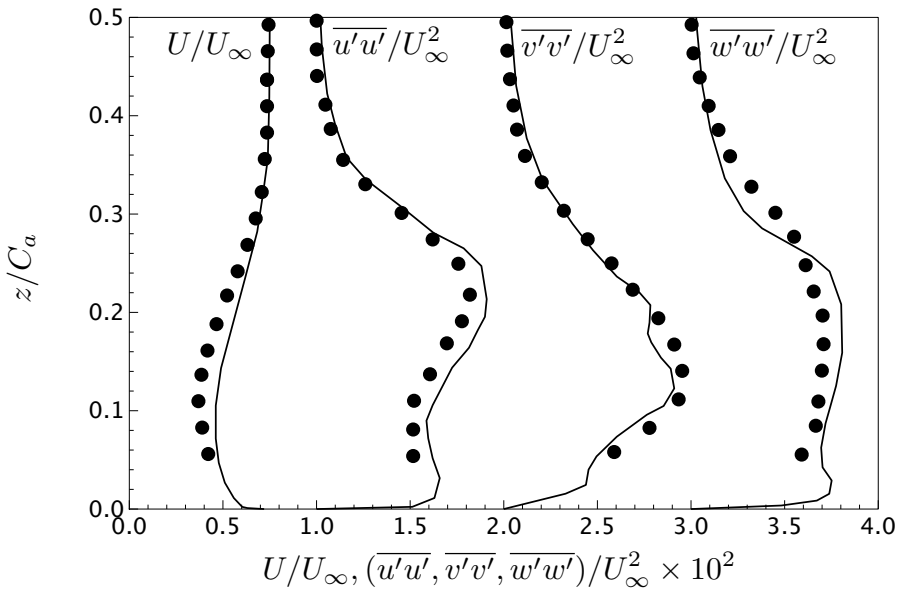

Figure 12. Profiles of the mean streamwise velocity (U/U_∞) and Reynolds normal stresses ($(\overline{u'u'}, \overline{v'v'}, \overline{w'w'})/U_\infty^2 \times 10^2$) along the spanwise direction at $(x/C_a, y/C_a) = (1.51, 1.35)$. ——, LES; ●, experiment [16]. The profiles of $\overline{u'u'}/U_\infty^2 \times 10^2$, $\overline{v'v'}/U_\infty^2 \times 10^2$, and $\overline{w'w'}/U_\infty^2 \times 10^2$ are shifted by 1, 2, and 3, respectively.

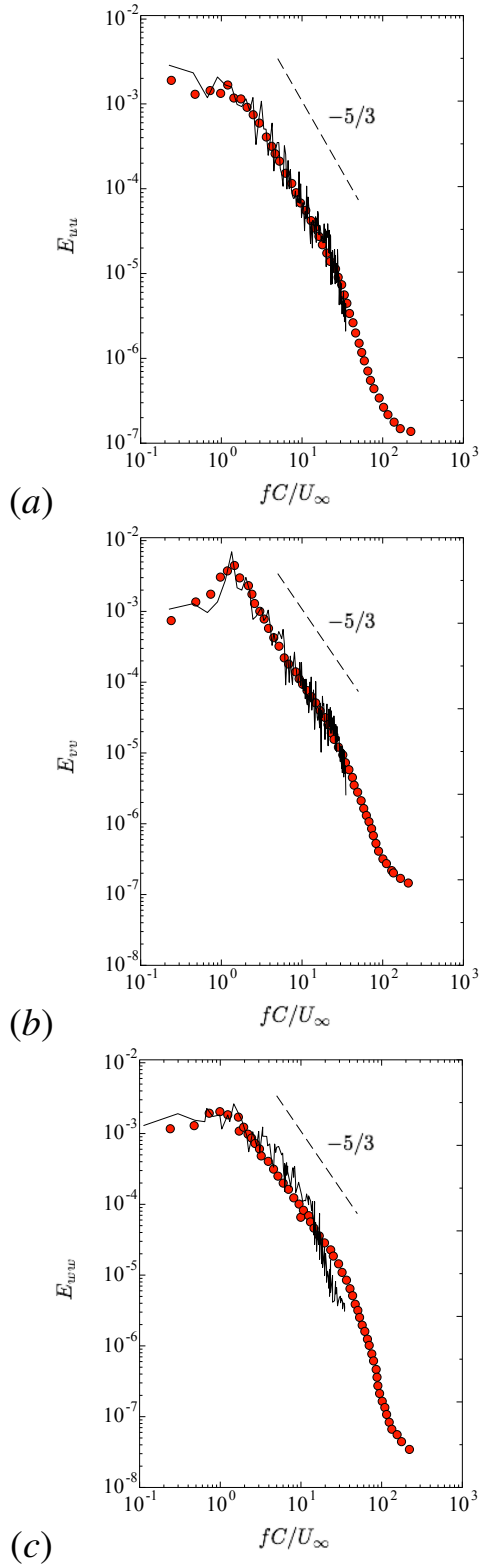

Figure 13. One-dimensional frequency spectra of velocity fluctuations at the location A in Fig. 11. (a) E_{uu}; (b) E_{vv}; (c) E_{ww}. ——— , LES; ● , experiment [16].

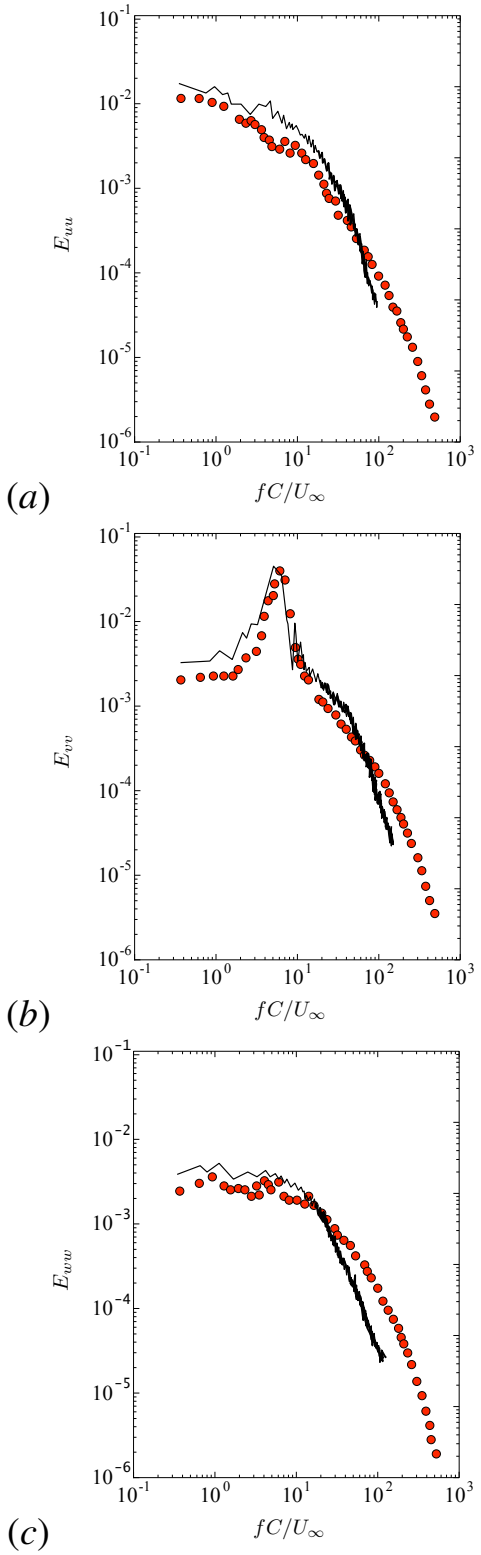

Figure 14. One-dimensional frequency spectra of velocity fluctuations in the blade wake at $x/C_a = 1.51, y/C_a = 2.2$ and $z/C_a = 0.9$. (*a*) E_{uu}; (*b*) E_{vv}; (*c*) E_{ww}. ——— , LES; ● , experiment [15].

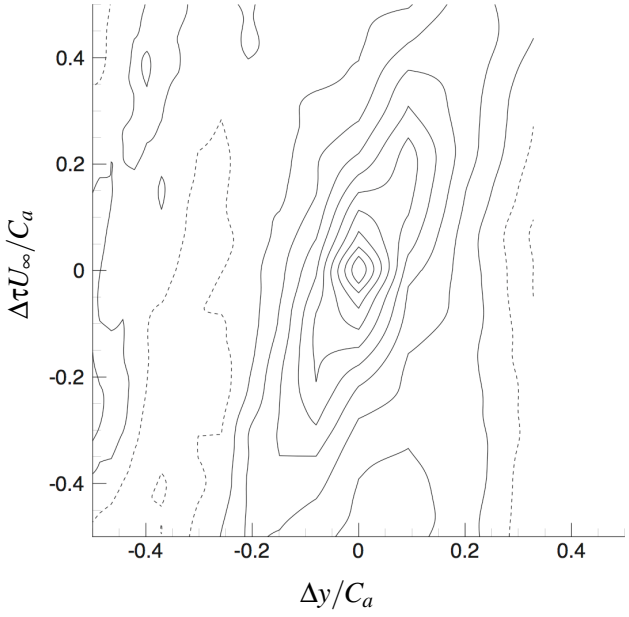

Figure 15. Contour plot of two-point correlations of the pitchwise velocity fluctuations as a function of the pitchwise spatial and temporal separations in the location A in Fig. 11. Contours are from -1 to 1 with increments of 0.1.

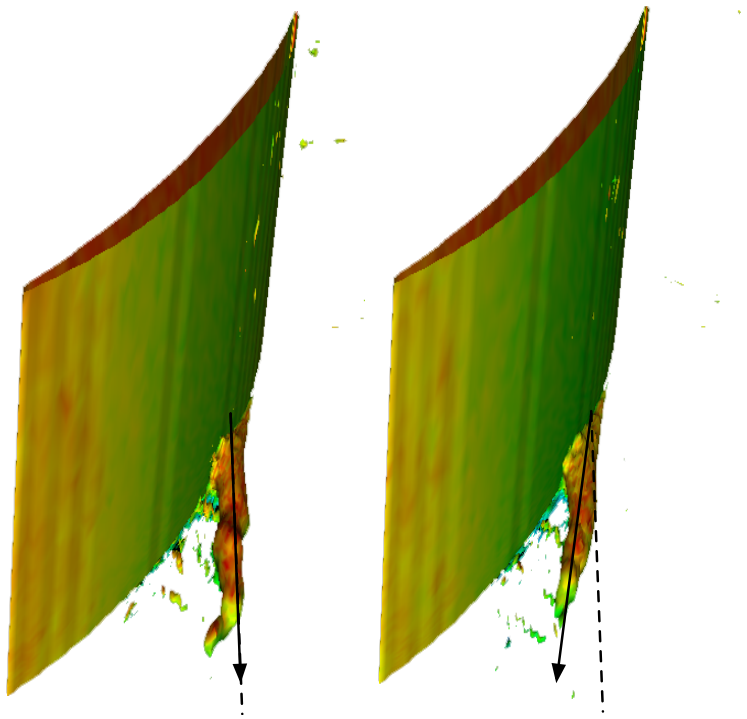

Figure 16. Instantaneous low pressure ($p/\rho U_\infty^2 = -0.2$) iso-surfaces showing a low-frequency wandering motion of the tip-leakage vortex. (*a*) t_0; (*b*) $t_0 + 0.33C/U_\infty$.

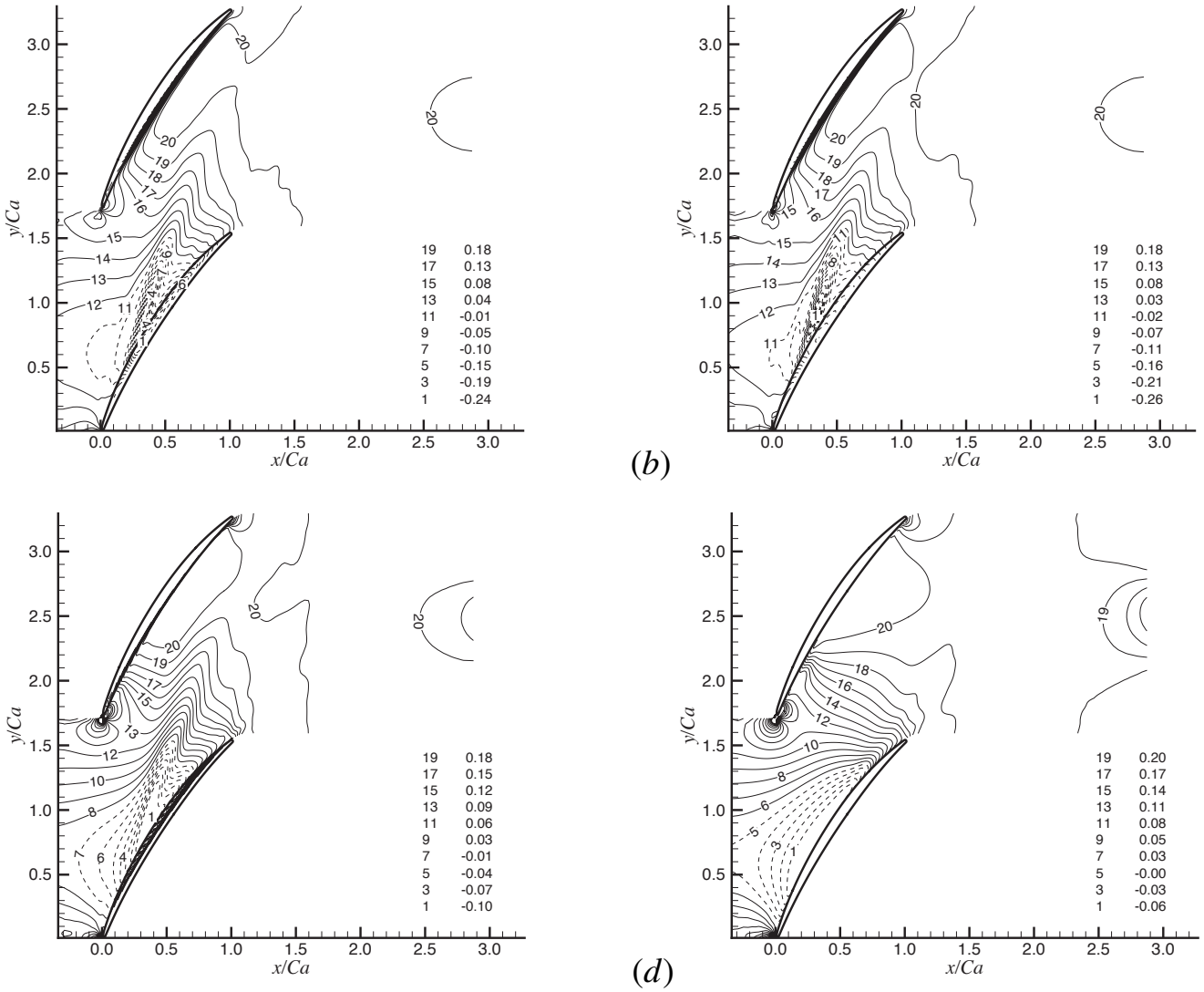

Figure 17. Contour plots of mean pressure in $y-z$ planes along the z-direction. (*a*) $z/C_a = 0.01$; (*b*) $z/C_a = 0.025$; (*c*) $z/C_a = 0.1$; (*d*) $z/C_a = 0.5$.

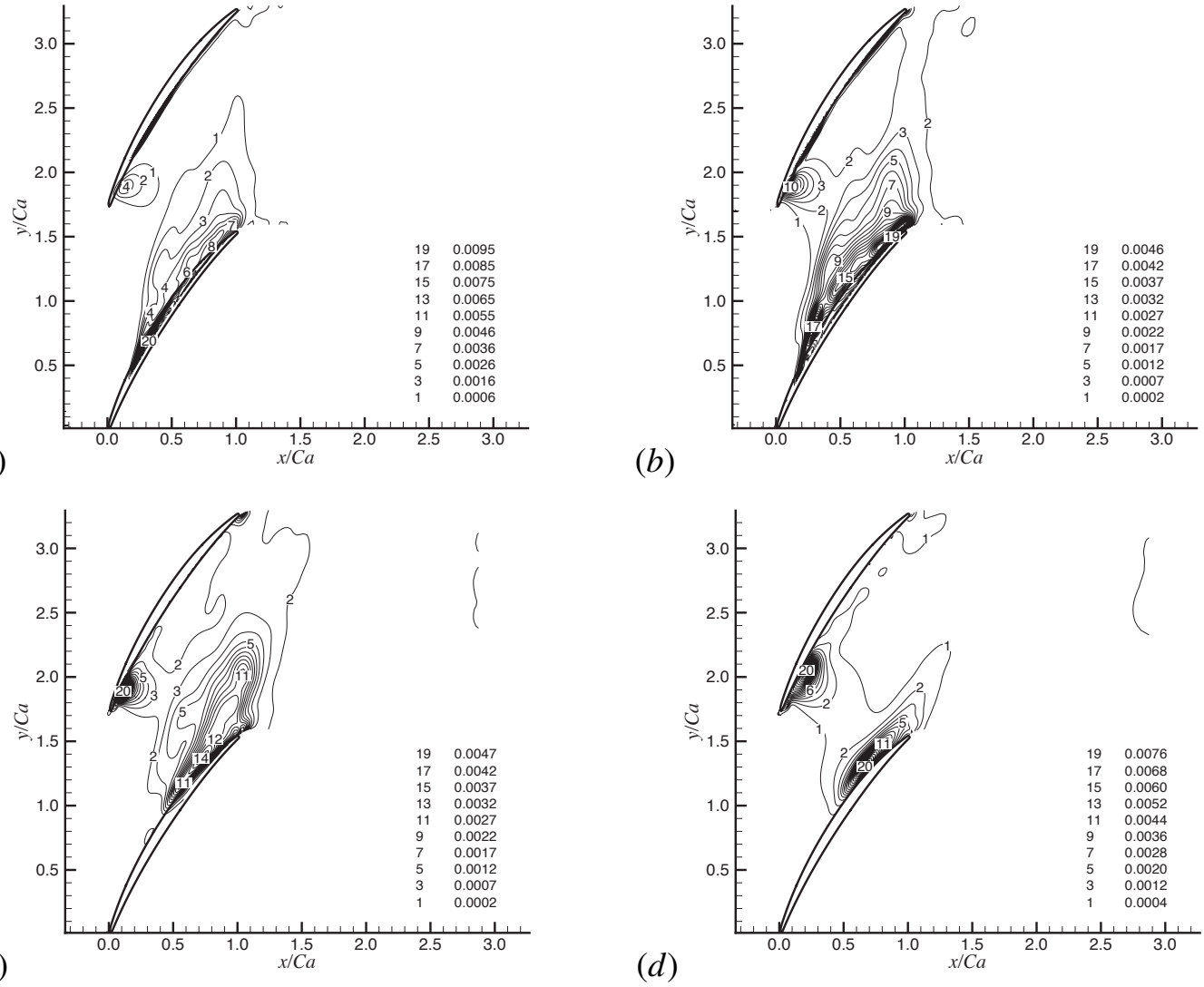

Figure 18. Contour plots of $\overline{p'p'}$ in $x-y$ planes along the z-direction. (*a*) $z/C_a = 0.01$; (*b*) $z/C_a = 0.025$; (*c*) $z/C_a = 0.1$; (*d*) $z/C_a = 0.5$.

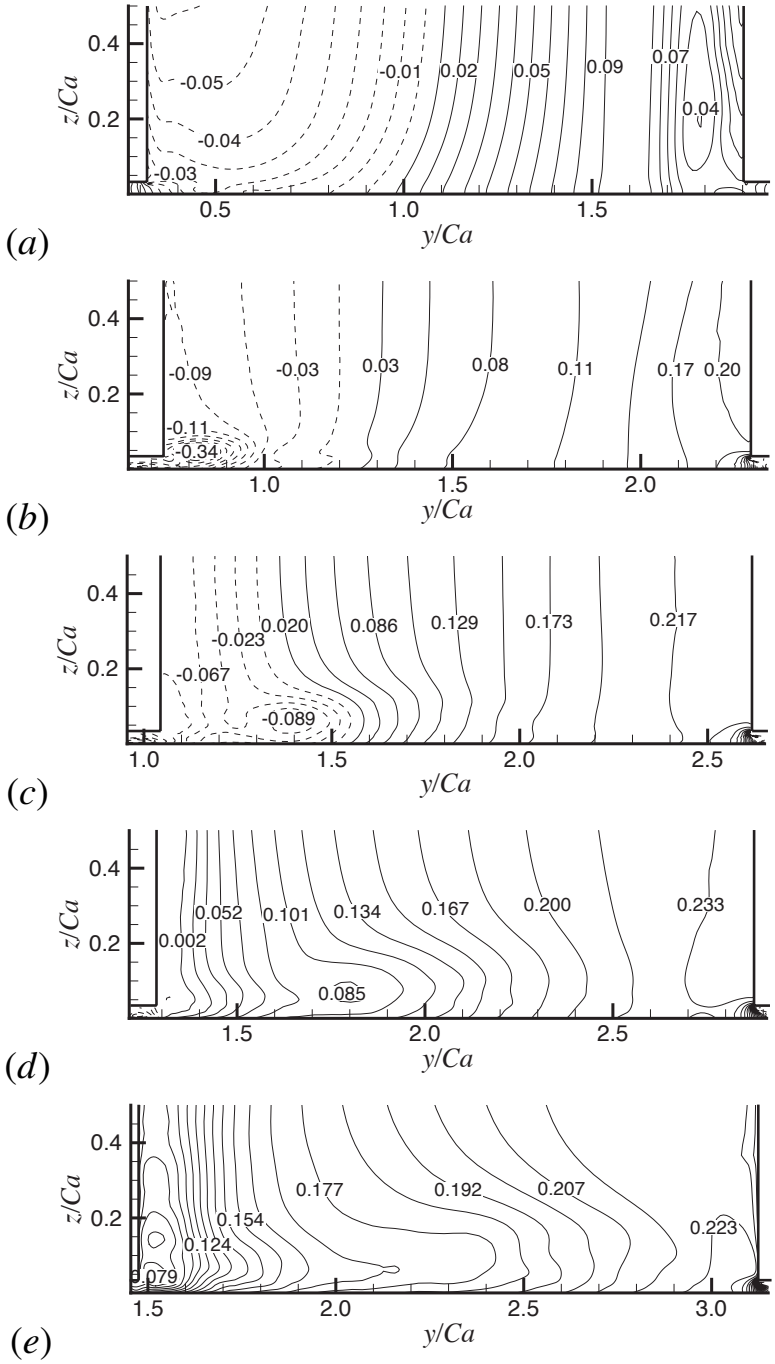

Figure 19. Contour plots of mean pressure in $y-z$ planes along the x-direction. (*a*) $x/C_a = 0.1$; (*b*) $x/C_a = 0.3$; (*c*) $x/C_a = 0.5$; (*d*) $x/C_a = 0.7$; (*e*) $x/C_a = 0.9$.

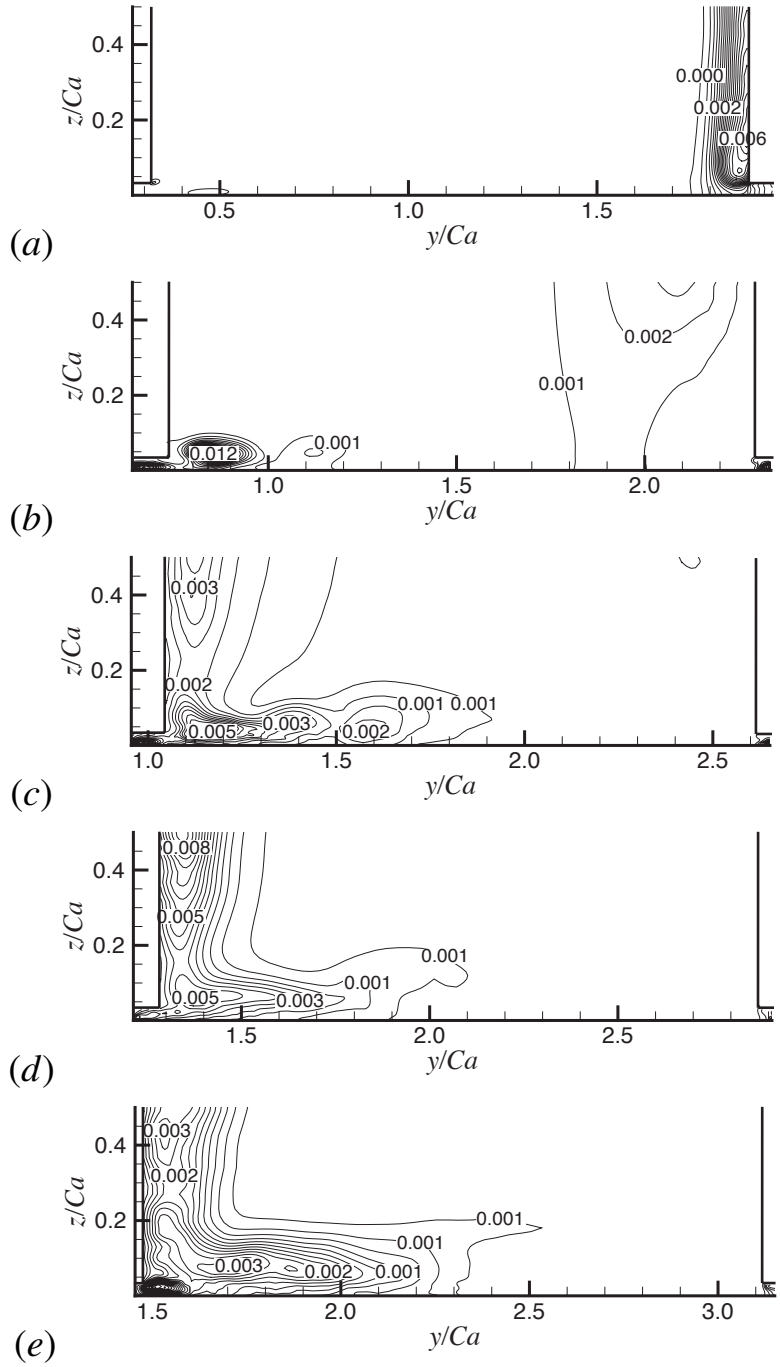

Figure 20. Contour plots of $\overline{p'p'}$ in $y-z$ planes along the x-direction. (*a*) $x/C_a = 0.1$; (*b*) $x/C_a = 0.3$; (*c*) $x/C_a = 0.5$; (*d*) $x/C_a = 0.7$; (*e*) $x/C_a = 0.9$.

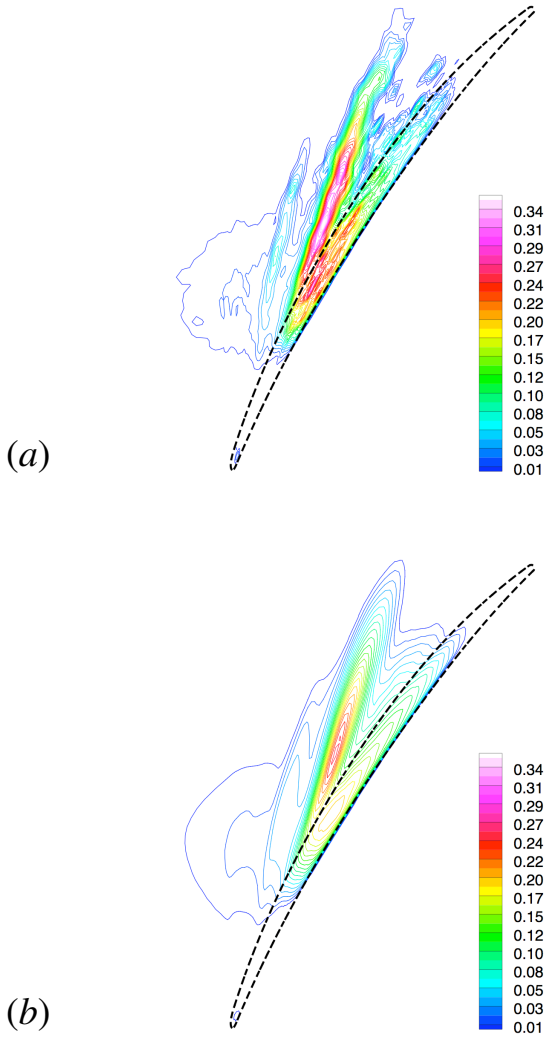

Figure 21. Contours of (a) instantaneous and (b) time-averaged cavitation criterion, $B = 1/3(B_{11} + B_{22} + B_{33})$, in a plane inside the tip gap at $z/C_a = 0.01$.